Cement clinker precursor production in an electrolyser

Zishuai Zhang,[1#] Benjamin A.W. Mowbray,[1#] Colin Parkyn[2], Chris Waizenegger,[1] Aubry S. R. Williams,[1] Eric W. Lees,[3] Shaoxuan Ren,[1] Yongwook Kim,[1]Ryan P. Jansonius,[1] Curtis P. Berlinguette[1,3,4,5*]

[1]Department of Chemistry, The University of British Columbia, 2036 Main Mall, Vancouver, British Columbia, V6T 1Z1, Canada.

[2]Department of Physics and Astronomy, University of Waterloo, 200 University Avenue West Waterloo, Ontario, Canada N2L 3G1

[3]Department of Chemical and Biological Engineering, The University of British Columbia, 2360 East Mall, Vancouver, British Columbia, V6T 1Z3, Canada.

[4]Stewart Blusson Quantum Matter Institute, The University of British Columbia, 2355 East Mall, Vancouver, British Columbia, V6T 1Z4, Canada.

[5]Canadian Institute for Advanced Research (CIFAR), 661 University Avenue, Toronto, M5G 1M1, Ontario, Canada.

[#] These authors contributed equally to this work

*Corresponding author: Curtis P. Berlinguette (cberling@chem.ubc.ca)

1. Methods

1.1 Faradaic efficiency calculation

We determined the Faradaic efficiency (*FE*) for reduction products (H_2 and CO) generated by the CO_2 reduction reaction (CO2RR) electrolyser while operating at constant current densities of 10, 20, and 30 mA cm^{-2}. We quantified *FE* values by measuring the concentration of H_2 and CO in the gaseous product stream using a gas chromatograph (GC) and determining the mole fraction of CO in the gaseous mixture, χ. The *FE* for each gaseous product *k* was then determined in accordance with Eq. S1:[1]

$$FE_k = \frac{n_k F \chi_k F_m}{I} \quad \text{Eq. S1}$$

Where n_k is the number of electrons exchanged ($n_{CO} = 2$), *F* is Faraday's constant (F = 96,485 C/mol), F_m is the molar flow rate in mol/s, and *I* is the total current in A. The molar flow rate is derived from the volumetric flow rate F_v by the relation $F_m = pF_v / RT$, where p is the atmospheric pressure in Pa, R is the ideal gas constant (8.314 J/mol K), and T is the temperature in degrees Kelvin. No liquid products were detected by ^{1}H NMR.

1.2 CO_2 utilization calculation

CO_2 utilization values were calculated in accordance with Eq. S2:

$$CO_2\ utilization = \frac{[CO]}{[CO_2]outlet + [CO]}\% \quad \text{Eq. S2}$$

This value represents the percentage of CO_2 fed to the CO2RR electrolyser that is converted into CO, and therefore the extent to which CO_2 emissions from the cement electrolyser are abated. [CO] and $[CO_2]_{outlet}$ represent the concentrations of CO and CO_2 in the gaseous outlet stream from the electrolyser as measured by in-line GC analysis.

1.3 Current efficiency calculation

Protons generated by the bipolar membrane (BPM) can either react with $CaCO_3$ in the chemical compartment (Eq. S3) or be transported across the cation-exchange membrane (CEM) and react with OH^- generated in the cathode compartment. We define the current efficiency as the percentage of protons generated by the BPM that react with $CaCO_3$ to form Ca^{2+} and CO_2 (Eq. S4).

$$CaCO_{3(s)} + 2H^+_{(aq)} \rightleftharpoons Ca^{2+}_{(aq)} + CO_{2(g)} + H_2O \quad \text{Eq. S3}$$

$$Current\ efficiency = \frac{Protons\ reacted\ with\ CaCO_3}{Total\ protons\ generated\ by\ the\ BPM}\ \% \quad \text{Eq. S4}$$

We determined the current efficiency of the cement electrolyser by measuring the flow rate (F_v) and concentration of the $CO_{2(g)}$ stream generated as a byproduct of $CaCO_3$ decomposition (Eq. S3). We then calculated the current efficiency according to Eq. S5:

$$Current\ efficiency = (F_m \chi)/(I/nF) \quad \text{Eq. S5}$$

Where F_m is the molar flow rate of gaseous species released from the chemical compartment of the cement electrolyser, χ is the mole fraction of CO_2 in this gaseous stream, I is the total current that passes through the electrode, n is the charge transfer number (n = 2 in this case), and F is Faraday's constant (F = 96,485 C/mol). The molar flow rate is derived from the volumetric flow rate F_v by the relation $F_m = pF_v / RT$, where p is the atmospheric pressure in Pa, R is the ideal gas constant (8.314 J/mol K), and T is the temperature in degrees Kelvin.

1.4 $Ca(OH)_{2(s)}$ Size and Morphology Characterization

We characterized the size and morphology of $Ca(OH)_{2(s)}$ particles formed during electrolysis at varying catholyte flow rates (50, 100, 300 and 500 ml min^{-1}) and a current density of 100 mA cm^{-2}, and at 100 and 200 mA cm^{-2} with a constant catholyte flow rate of 300 ml min^{-1}. After 60 min at each set of

conditions, $Ca(OH)_{2(s)}$ samples were carefully collected from the cathode compartment, rinsed with DI water and dried in a fume hood overnight before characterization by SEM.

Our preliminary results indicate the catholyte flow rate has a significant impact on the morphology of $Ca(OH)_{2(s)}$ particles. At the lowest flow rate (50 ml min^{-1}) hexagonal prism shaped crystallites were observed, whereas aggregates of smaller spherical particles were observed at flow rates > 100 ml min^{-1}. The size of $Ca(OH)_{2(s)}$ particles was observed to decrease with increasing catholyte flow rates. We reason that this observation is caused by increased shear forces in the liquid electrolyte at higher flow rates which creates less favorable crystallite growth conditions.[2] This result suggests that the size of $Ca(OH)_{2(s)}$ particles can be tuned by modulating the catholyte flow rate. We also investigated how current density affects the morphology of $Ca(OH)_{2(s)}$ and found that a higher current density (200 mA cm^{-2}) causes $Ca(OH)_{2(s)}$ to form in less defined shapes and morphologies. We speculate that the poorly-defined morphology of $Ca(OH)_{2(s)}$ formed at current densities >100 mA cm^{-2} could be caused by rapid rates of $H_{2(g)}$ bubble evolution on the cathode surface which disturbs crystallite growth. All $Ca(OH)_{2(s)}$ particles formed in these experiments were much smaller than the typical <90 μm size specification for raw mixtures in cement production.[3]

1.5 $Ca(OH)_2$ deposition on cathodes and cation-exchange membrane (CEMs)

We measured the accumulation of $Ca(OH)_2$ on the Ni cathode and cation exchange membrane (CEM) by measuring the mass of each component before and after electrolysis. For the cathode, the mass of a pristine, dry, Ni foam cathode was measured and defined as m_1, and the mass of the electrode after 1 h electrolysis at 100 mA cm^{-2} was measured and defined as m_2. The theoretical yield of $Ca(OH)_2$ produced during this experiment was calculated to be 486 mg. This value was used as the denominator to calculate the percentage of $Ca(OH)_2$ product that accumulates on the cathode according to Eq. S6:

$$Ca(OH)2\ deposition\ percentage = (m2 - m1)/486\ mg\ (\%) \quad \text{Eq. S6}$$

The deposition of $Ca(OH)_2$ on the CEM was calculated using the same method.

2. Life-cycle analysis

We performed a life-cycle analysis (LCA) of the energy, emissions, and operating costs associated with the manufacture of cement for both electrochemical and incumbent thermal pathways. This analysis calculates the total energy to make Portland cement (95% clinker, 5% $CaSO_4$) based on: i) the performance metrics of the cement electrolyser (voltages, current density, and current efficiency); ii) the energy demand of the high-temperature kilns which generate clinker (assumed to be 65 wt% CaO); and iii) and the electricity demand of auxiliary equipment for processing the $CaCO_{3(s)}$ feedstock and clinker product (Figure S12, S13). The emissions for each production pathway were calculated based on the carbon intensity of electricity generation and kiln fuels. We estimated operating costs based on the cost of electricity, kiln fuels, and a carbon tax based on carbon pricing in the Inflation Reduction Act recently passed in the United States. We compared the energy, emissions, and operating costs of electrochemical cement production to incumbent thermal methods using a set of parameters which represent a forward-looking cost-parity scenario (Table 1). We also assessed the sensitivity of the operating cost for electrochemical cement to key parameters varied between three levels: pessimistic; median; and optimistic (Table 1). The results of these analyses are described in the main text.

Calculation of energy consumption:

The energy consumption for electrochemical cement production was calculated using the voltage and current efficiency of the cement electrolyser, the energy demand of the $Ca(OH)_{2(s)}$-fed kiln, and the electricity demand of auxiliary equipment (90 kWh/tonne cement).[4] Electrolyser performance metrics were selected based on experimental results: we assume a cell voltage of 2.5 V and 100% current efficiency in the forward-looking scenario. For the sensitivity analysis, the voltage and current efficiency were varied from 2-4 V and 70-100%, respectively. The energy demand of the $Ca(OH)_{2(s)}$-fed kiln was calculated by adjusting the energy demand of a reference $CaCO_{3(s)}$-fed kiln for the difference in free

energy between the decomposition of $Ca(OH)_{2(s)}$ and $CaCO_{3(s)}$ into CaO (and H_2O or CO_2). The calculated energy demand of the $Ca(OH)_{2(s)}$-fed kiln (2.8 GJ/tonne cement) therefore represents the sum of the thermodynamic energy to decompose $Ca(OH)_2$ into CaO and H_2O (139 kJ/mol CaO at 900 °C) and the additional energy required to convert CaO and SiO_2 into clinker [assumed to be 45% of the energy consumed by the $CaCO_{3(s)}$-fed kiln[5]]. The free energy to decompose $Ca(OH)_2$ into CaO and H_2O at 900 °C was determined using the fundamental relationship $\Delta G = \Delta H - T\Delta S$, where ΔH and ΔS at 900 °C were calculated according to the thermodynamic cycle depicted in Scheme S1.[6] Our analysis indicates that combustion of $H_{2(g)}/O_{2(g)}$ streams released from the cement electrolyser with 88% efficiency would provide sufficient thermal energy to heat the $Ca(OH)_{2(s)}$-fed kiln. In this scenario, cement production would be driven entirely using electricity (Figure S14). For the sensitivity analysis, we varied the $H_{2(g)}/O_{2(g)}$ combustion efficiency between 70-90% and assumed that any additional thermal energy required would be sourced from the combustion of hydrocarbon fuels. The energy demand for thermal cement production was extracted from reference datasets which detail the energy consumption of cement manufacturing.[4,7–9] We assumed the energy demand of the $CaCO_{3(s)}$-fed kiln to be 3.1 GJ/tonne cement in the forward-looking scenario,[10] and varied this value from 3.1-2.7 GJ/tonne cement in the sensitivity analysis.[4,7]

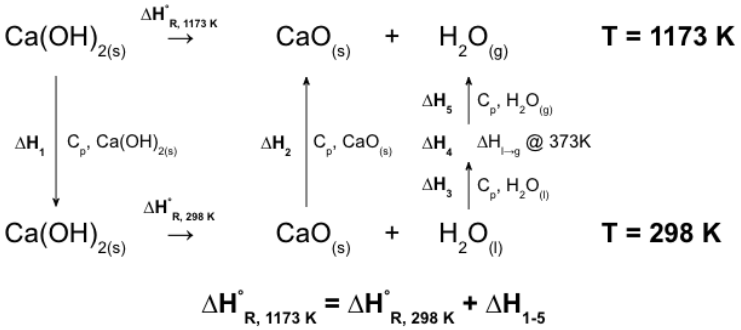

Scheme S1. Schematic representation of the thermodynamic cycle used to calculate the enthalpy of reaction for the thermal decomposition of $Ca(OH)_{2(s)}$ at 900 °C.[6] Enthalpies for each step were calculated using heat capacity (C_p) values from literature.[6] The entropy of reaction was also calculated for the same thermodynamic cycle using the appropriate equations.

Calculation of CO_2 emissions:

CO_2 emissions were calculated based on the carbon intensity of electricity generation and fuels used to heat the high-temperature kiln. For the electrochemical pathway, we assumed 100% utilization of CO_2 released from the electrolyser in the forward-looking scenario, and varied this value from 50-90% in the sensitivity analysis. Electricity generation in the forward-looking scenario was assumed to be sourced from a low-carbon grid with an emissions intensity factor similar to the national average for electricity generation in Canada (0.150 kg CO_2/kWh).[11] For the sensitivity analysis, the emissions intensity of electricity generation was varied from 0.100 kg CO_2/kWh to 0.250 kg CO_2/kWh (comparable to the intensity of electricity generation in the UK). Emissions from heating the high-temperature kiln were calculated using widely reported emissions factors for commonly used kiln fuels.[12] In the forward-looking scenario, the kiln fuel was assumed to be natural gas (CH_4). In the pessimistic scenario of the sensitivity analysis, the emissions intensity of the kiln fuel was calculated as a weighted average based on current kiln fuel use in Canada.[12] The kiln fuels used in median and optimistic scenarios were natural gas (CH_4) and hydrogen (H_2), respectively.

Calculation of operating costs:

The operating costs for electrochemical and thermal cement production were calculated based on the cost of electricity, kiln fuels, and emitted CO_2 (i.e., a carbon tax). For the cost of electricity in the sensitivity analysis, we adopted widely used assumptions for future market conditions and varied the price of electricity from \$0.03-0.10/kWh.[13,14] In the forward-looking scenario we used an electricity price of \$0.03/kWh.[15] The price of kiln fuels was calculated based on short-term projections of market prices.[16] To account for the price of emitted CO_2, we incorporated a carbon tax varying from \$60-110/tonne of CO_2, and used the value of \$85/tonne of CO_2 in the forward-looking scenario to align with pricing in the Inflation Reduction Act.

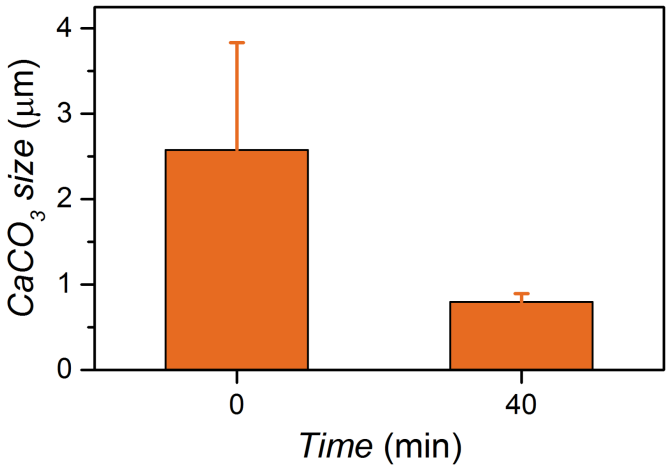

Figure S1. Change in $CaCO_3$ particle size before and after 40 minutes of electrolysis at 50 mA cm^{-2}. $CaCO_3$ particle size was measured by dynamic light scattering (DLS).

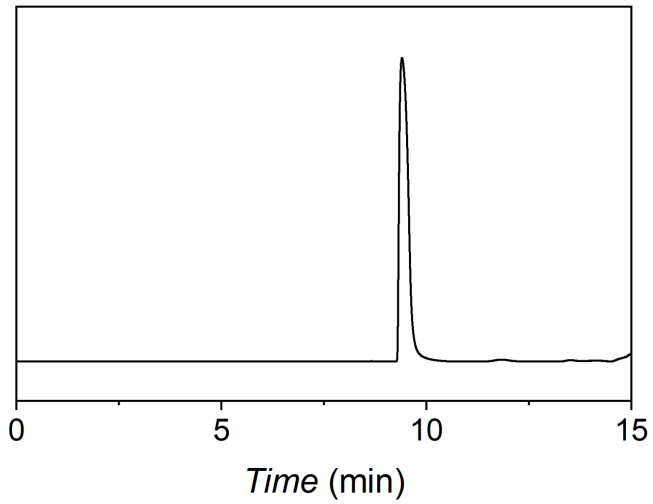

Figure S2. Gas chromatography (GC) analysis of the gaseous stream released from the chemical compartment of the cement electrolyser. CO_2 was the only species detected by the flame ionization detection (FID) on the in-line GC.

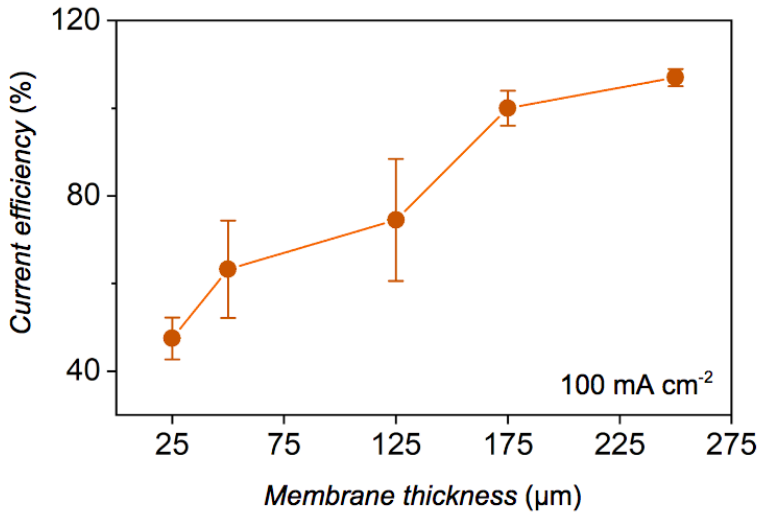

Figure S3. Effect of cation exchange membrane (CEM) thickness on current efficiency. Current efficiency measurements are described in the Supplementary Materials Section 1.3. The CEMs used in these experiments were commercially available Nafion membranes with thicknesses of 25, 50, 125, 175 and 250 µm.

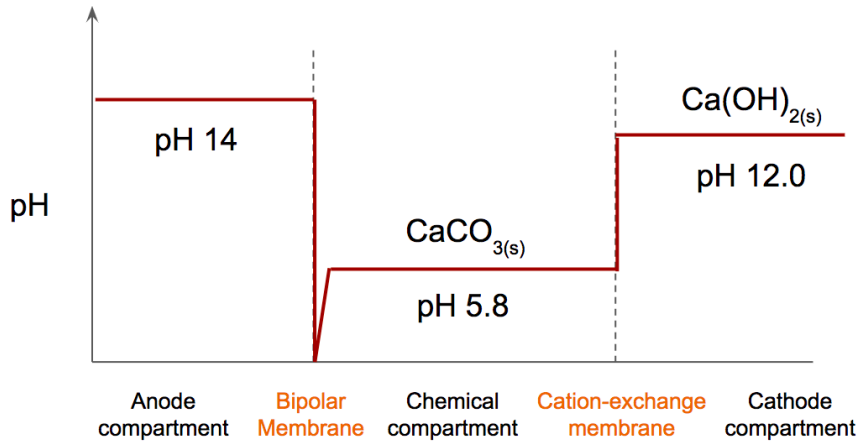

Figure S4. pH profile of anode, chemical and cathode compartments during electrolysis at 100 mA cm^{-2}. Measurements were taken after 20 minutes of electrolysis. The pH values were <1.0 and >14.0 respectively before $CaCO_3$ was added to the chemical compartment.

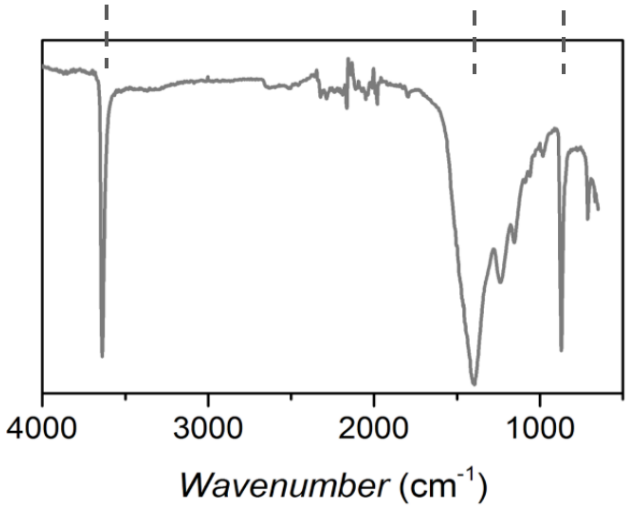

Figure S5. Fourier-transform infrared spectroscopy (FTIR) of the $Ca(OH)_2$ generated in the cathode compartment. Dashed lines correspond to characteristic peaks of $Ca(OH)_2$ at 3647, 1428 and 876 cm^{-1}.[17]

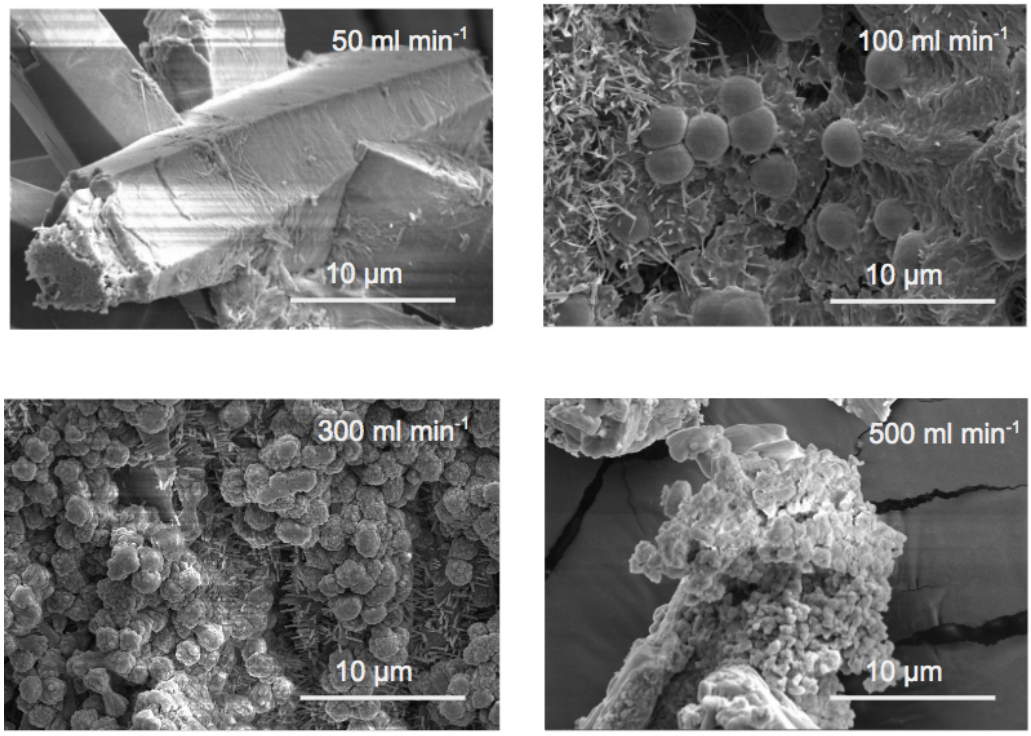

Figure S6. Scanning electron microscopy (SEM) images of $Ca(OH)_{2(s)}$ generated at catholyte flow rates of 50, 100, 300 and 500 ml min^{-1}. Crystallites isolated from experiments with a catholyte flow rate of 50 ml min^{-1} were found to be hexagonal prisms ~10-40 microns in size. At flow rates >50 ml min^{-1} the $Ca(OH)_{2(g)}$ morphology changed to aggregates of smaller spherical crystallites <10 microns in size. A constant current density of 100 mA cm^{-2} was used for all experiments.

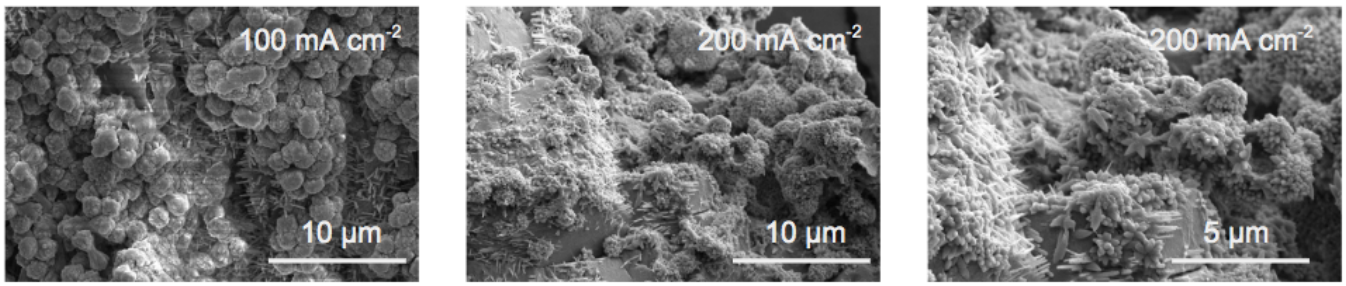

Figure S7. Scanning electron microscopy (SEM) images of $Ca(OH)_{2(s)}$ generated at current densities of 100 and 200 mA cm^{-2} and a constant flow rate of 300 ml min^{-1}. At 100 mA cm^{-2} the morphology of $Ca(OH)_{2(s)}$ crystallites was reasonably well-defined as aggregates of spherical particles <10 microns in size. At 200 mA cm^{-2}, the shape of these aggregates was less defined and the size of individual crystallizes decreased below <1 micron.

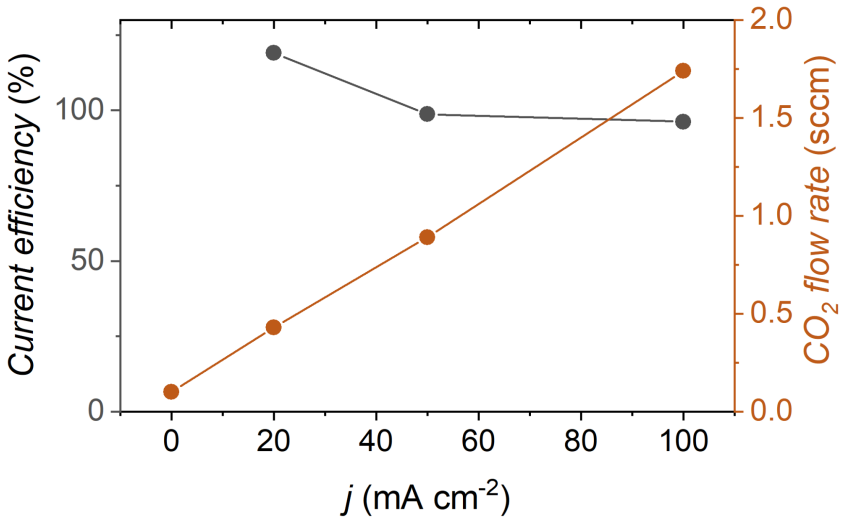

Figure S8. CO_2 flow rate (orange) and current efficiency (grey) of the cement electrolyser as a function of current density (j). The flow rate of CO_2 released from the cement electrolyser was measured using a digital flow meter. The concentration of CO_2 in this stream was measured using an in-line gas chromatograph (GC). Current efficiency calculations were performed according to the procedure described in the Supplementary Materials Section 1.3.

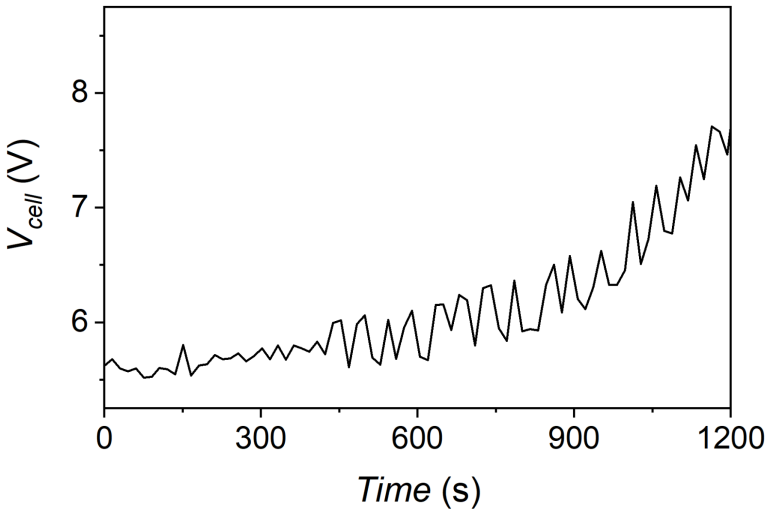

Figure S9. Voltage-time characteristics of the cement electrolyser operating at 100 mA cm^{-2}. The cell voltage (V_{cell}) notably increases during electrolysis due to the accumulation of $Ca(OH)_2$ on the cathode and CEM. The magnitude of the voltage increase varies between experiments, a representative voltage-time curve is shown here.

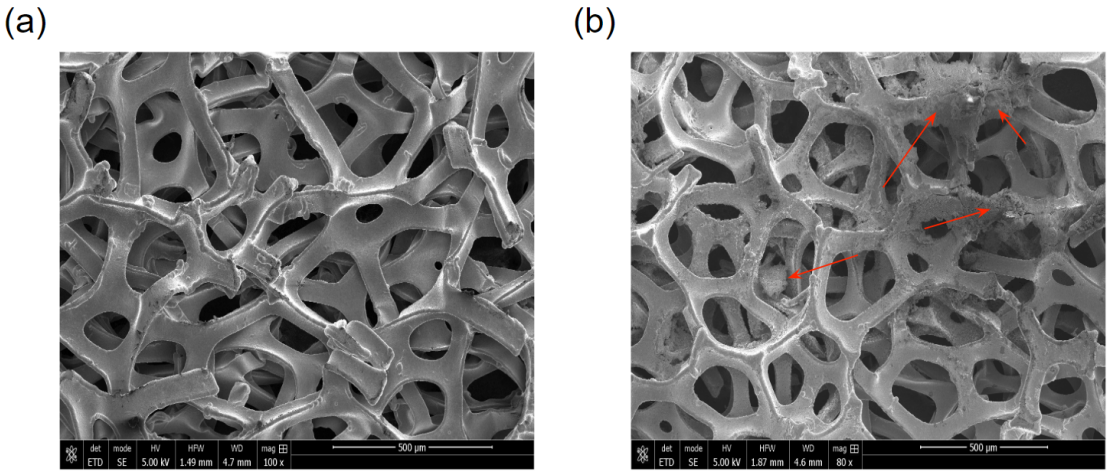

Figure S10. Scanning electron microscopy images of the Ni foam cathode before and after electrolysis. The slight accumulation of ($Ca(OH)_{2(s)}$, red arrows) can be observed on the surface of the electrode after electrolysis.

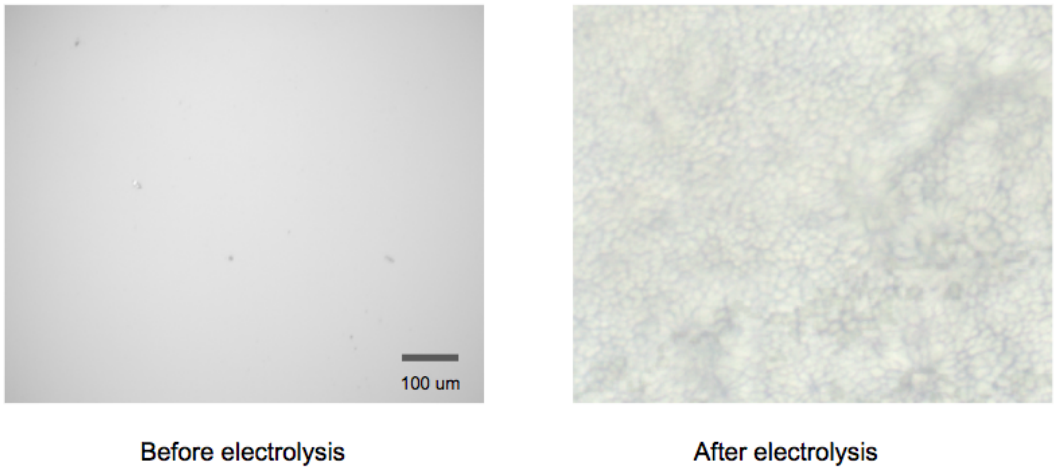

Figure S11. Optical microscopy images of the Nafion membrane before and after 1 h of electrolysis at 100 mA cm^{-2}. Micro-clusters of precipitated $Ca(OH)_{2(s)}$ are observed on the surface of Nafion after electrolysis.

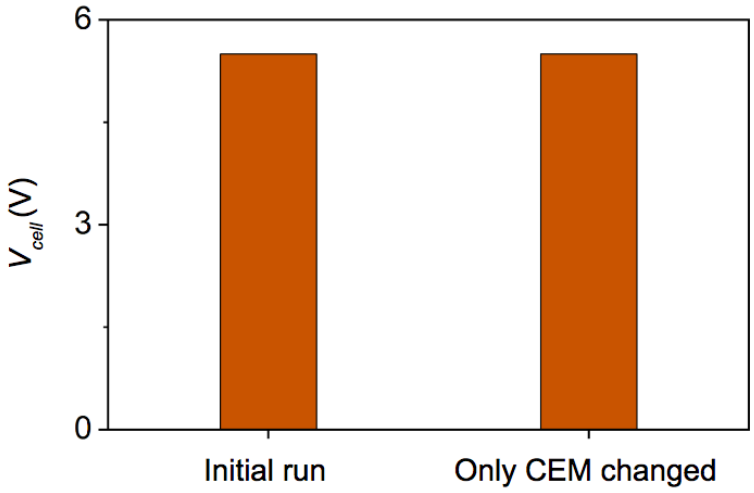

Figure S12. Cell voltage (V_{cell}) of the cement electrolyser at the onset of electrolysis (t = 0) and after replacing the cation exchange membrane (CEM) after 1 h of electrolysis. The initial V_{cell} value at 100 mA cm^{-2} was 5.5 V, but increased to ~8V over 1 h of electrolysis (e.g., Figure S6). The V_{cell} was restored to the initial value of 5.5 V replacing the CEM and leaving the cathode unchanged. This result indicates that the V_{cell} increases largely due to the deposition of $Ca(OH)_2$ on the CEM surface.

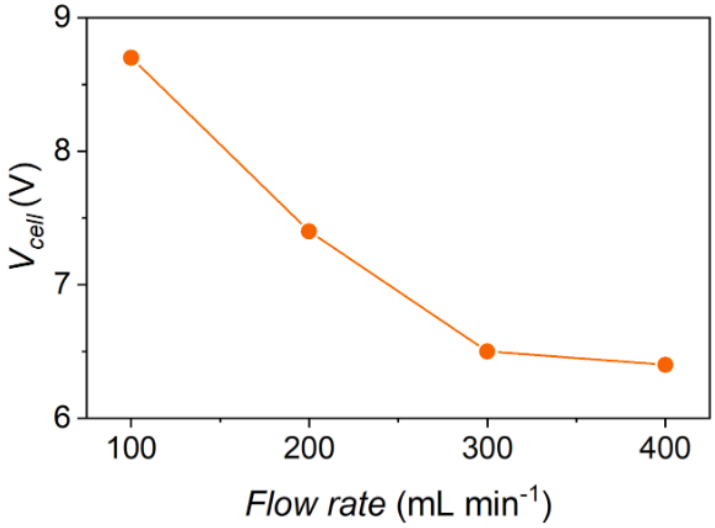

Figure S13. Influence of solution flow rate on cell voltage (V_{cell}). Solutions were fed to the anode, chemical and cathode compartments at the same rate to minimize pressure gradients across the membranes. Based on these results, we used 300 mL min^{-1} as the flow rate for this study. Experiment conditions: T = 20 °C; electrode mass ~0.6 g for both anode and cathode; membranes = Fumasep FBM BPM and Nafion 117.

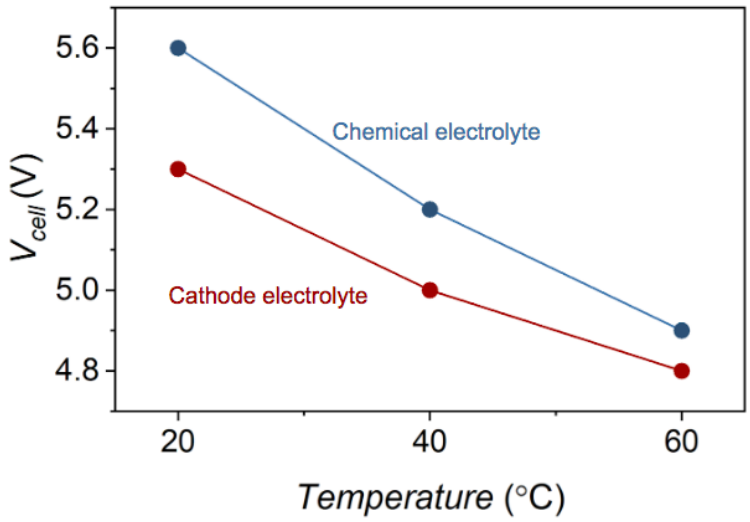

Figure S14. Effect of cathode and chemical compartment electrolyte temperature on cell voltage (V_{cell}). For these experiments, the temperature of the cathode or chemical compartment electrolyte was increased while the other was kept at room temperature, and vice versa. Experiment conditions: electrode mass is ~0.6 g for both anode and cathode; electrolyte flow rate for anolyte, catholyte and chemical compartments = 300 mL min^{-1}. Membranes = Fumasep FBM BPM and Nafion 117.

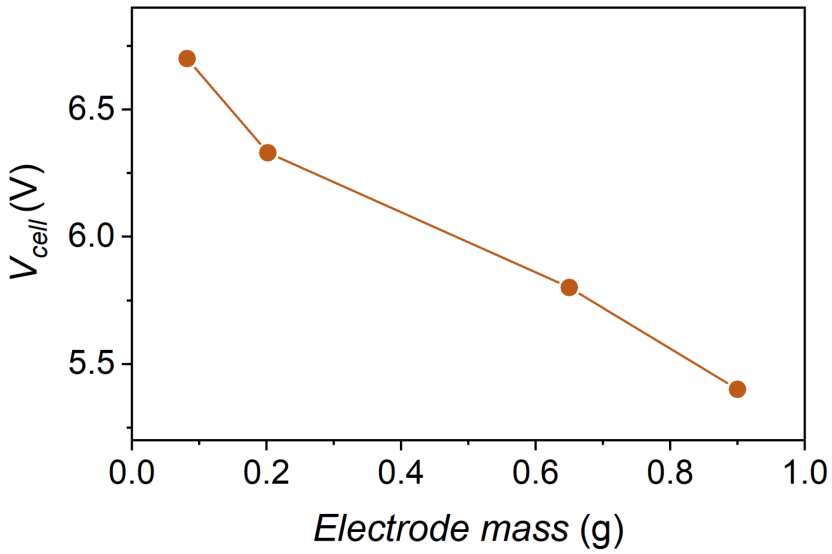

Figure S15. The influence of electrode mass (i.e., loading) on cell voltage (V_{cell}). Electrode mass values correspond to both the anode and cathode loadings: 0.9 g represents the maximum mass of Ni foam that can be housed in either the anode and cathode compartment. Experimental conditions: T = 20 ℃; electrolyte flow rate for anolyte, catholyte and chemical compartments = 300 mL min^{-1}; membranes = Fumasep FBM BPM and Nafion 117.

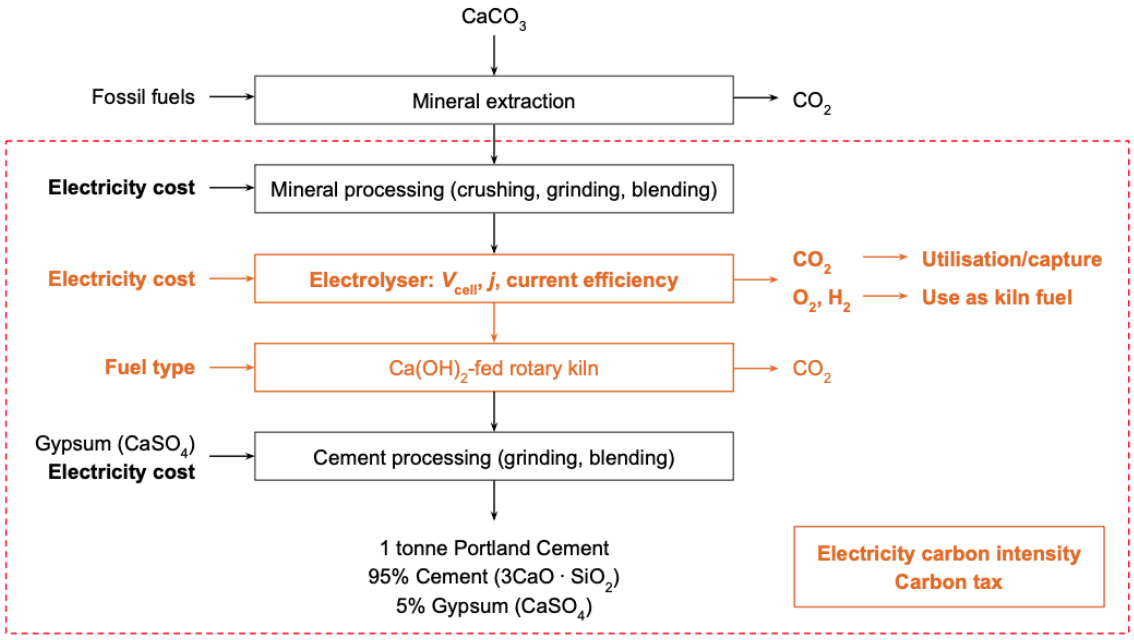

Figure S16. Scope of life-cycle analysis of the energy, emissions, and operating costs associated with electrochemical cement production. Parameters manipulated between different scenarios are indicated in bold.

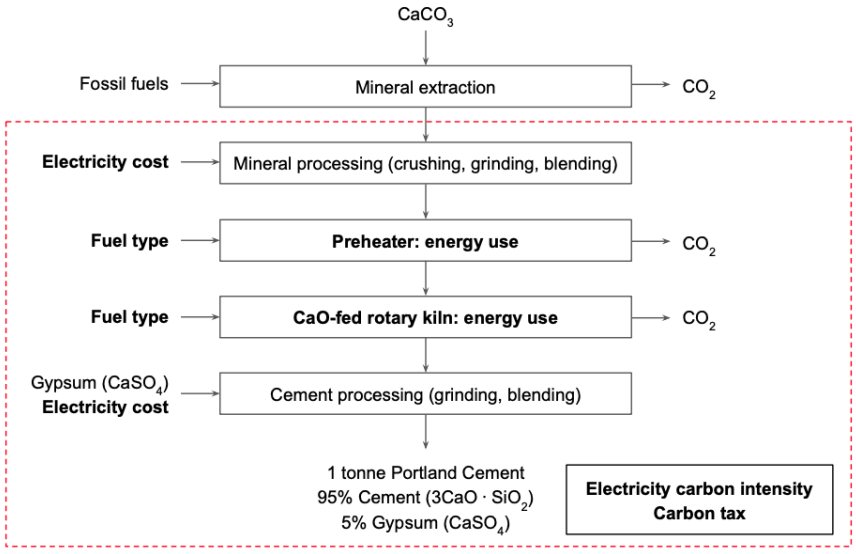

Figure S17. Scope of life-cycle analysis of the energy, emissions, and operating costs associated with conventional thermal cement production. Parameters manipulated between different scenarios are indicated in bold.

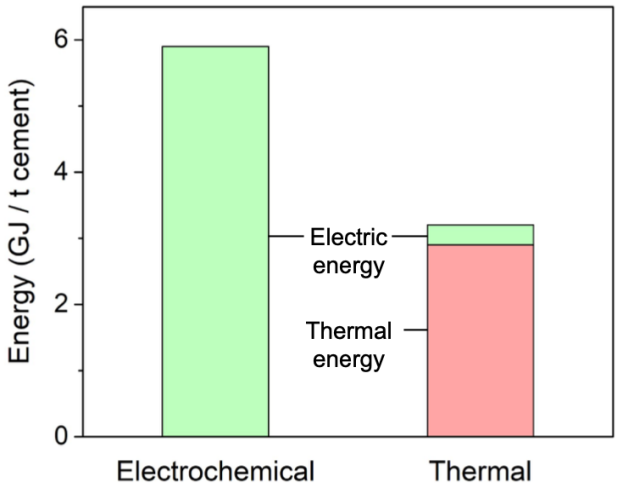

Figure S18. Analysis of energy consumption for electrochemical cement and thermal cement. Comparison of energy consumption for electrochemical and thermal cement in a forward-looking cost-parity scenario detailed in Table 1 [electricity price = \$0.02 / kWh, cell voltage = 2.5 V, current efficiency = 100%, grid emissions intensity = 0.100 kg CO_2 / kWh, carbon tax = \$50 / tonne CO_2, H_2/O_2 combustion efficiency = 88%, kiln fuel (thermal pathway) = CH_4]. This analysis assumes that $H_{2(g)}/O_{2(g)}$ streams are combusted as a source of thermal energy for a $Ca(OH)_{2(s)}$-fed kiln.

References:

1 D. A. Salvatore, D. M. Weekes, J. He, K. E. Dettelbach, Y. C. Li, T. E. Mallouk and C. P. Berlinguette, *ACS Energy Lett.*, 2018, **3**, 149–154.
2 W. R. Wilcox, *Prog. Cryst. Growth Charact. Mater.*, 1993, **26**, 153–194.
3 L. D. Ellis, A. F. Badel and M. L. Chiang, *Proceedings of the National Academy of Sciences of the United States of America*, 2020, **117**, 12584–12591.
4 International Energy Agency, *Cement Technology Roadmap: Carbon Emissions Reductions up to 2050*, IEA, 2009.
5 Y. K. Verma, B. Mazumdar and P. Ghosh, *Environmental Engineering Research*, , DOI:10.4491/eer.2020.111.
6 J. J. Beaudoin, T. Sato and P. J. Tumidajski, *2nd International Symposium on Advances in Concrete Through Science and Engineering*, 2006, 1–15.
7 International Energy Agency, *Tracking industrial energy efficiency and CO2 emissions*, IEA, 2007.
8 E. Worrell, L. Price, N. Martin, C. Hendriks and L. and Ozawa Meida, *Annual Review of Energy and the Environment*, 2001, **26**, 303–329.
9 Natural Resources Canada, *Energy Consumption: Benchmark Guide - Cement Clinker Production*, .
10 D. R. Nhuchhen, S. P. Sit and D. B. Layzell, *Appl. Energy*, 2022, **317**, 119180.
11 Carbon intensity of electricity, https://ourworldindata.org/grapher/carbon-intensity-electricity (Accessed July 12, 2022), (accessed 11 July 2022).
12 M. E. Boesch and S. Hellweg, *Environ. Sci. Technol.*, 2010, **44**, 9143–9149.

13 M. Jouny, W. Luc and F. Jiao, *Ind. Eng. Chem. Res.*, 2018, **57**, 2165–2177.
14 Z. Huang, R. Gary Grim, J. A. Schaidle and L. Tao, *Energy Environ. Sci.*, 2021, **14**, 3664–3678.
15 R. H. Wiser and M. Bolinger, .
16 U.S. Energy Information Administration, *Short-Term Energy Outlook - June 2022*, U.S. Energy Information Administration.
17 S. Tanpure, V. Ghanwat, B. Shinde, K. Tanpure and S. Lawande, *Polycycl. Aromat. Compd.*, 2022, **42**, 1322–1340.